Electronic reconstruction in confined $SrRuO_3$ monolayers

U. Lamichhane,[1,*] B. Sankhi,[1] N. Kundu,[1] G. Fabbris,[2] Y. Choi,[2] D. Haskel,[2] J. L. McChesney,[2] Yue Cao,[3] J. Li,[4] V. Bisogni,[4] M. F. Borunda,[1] and D. Meyers[1,†]

[1]*Department of Physics, Oklahoma State University, Stillwater, Oklahoma 74078, USA*

[2]*Advanced Photon Source, Argonne National Laboratory, Lemont, Illinois 60439, USA*

[3]*Materials Science Division, Argonne National Laboratory, Lemont, Illinois 60439, USA*

[4]*NSLS-II, Brookhaven National Laboratory, Upton, New York 11973, USA*

(Received 3 May 2024; revised 6 November 2024; accepted 13 November 2024; published 2 December 2024)

We report the observation of an electronic reconstruction in dimensionally controlled ruthenate heterostructures synthesized by pulsed laser deposition. High structural and electronic quality of superlattices comprised of a single $SrRuO_3$ layer inter-spaced with varying thicknesses of insulating $SrTiO_3$ layers was verified by reflection high energy electron diffraction, atomic force microscopy, x-ray diffraction, reciprocal space mapping, and x-ray absorption spectroscopy. X-ray absorption spectroscopy evidences a confinement-driven evolution of the Ru electronic configuration from the $d^5\underline{L}$ to the d^4 state. Significant increases of the spin-orbit coupling are observed in connection with the configuration changes supporting recent works identifying large enhancement of the magnetic anisotropy. The growth of high quality two-dimensional confined ruthenate layers under precisely controlled environments highlights the potential to directly manipulate interlayer coupling and selectively perturb the electronic state in ruthenates in analogy to superconducting Sr_2RuO_4.

DOI: 10.1103/PhysRevB.110.235104

I. INTRODUCTION

Complex transition metal oxides with strongly correlated carriers have attracted vast attention in condensed matter physics due to their exciting phenomena such as high-temperature superconductivity, temperature driven metal to insulator transition, frustrated magnetism, and colossal magnetoresistance [1–8]. With the development of advanced synthesis techniques, the growth of high-quality thin films has added more avenues for exploring this research area due to the various tuning parameters introduced [9–11]. Furthermore, complex oxide superlattices (SLs) exhibit remarkable physical phenomena emerging at the interface, which can be unattainable in bulk constituents [12,13]. These layered materials exhibit an astonishing dimensionality dependence of physical properties due to the delicate control of the oxide interface at the atomic scale. To obtain these emergent characteristics, extensive investigations have been undertaken in recent years [13–21].

Concurrent with the rise of oxide heterostructuring, ruthenium-based perovskite systems have been at the forefront of materials physics research because of their unique properties [22–30]. The discovery of unconventional superconductivity in layered perovskite Sr_2RuO_4 (S2RO4) [31] generated great excitement and drove decades of research. Due to its potential topologically nontrivial pairing symmetry, S2RO4 is considered a candidate for odd parity superconductor-based quantum computing [32–34]. The unconventional superconductivity in this system has been extensively studied, but the true nature of the pairing mechanism remains elusive [35,36]. Recent experiments have cast significant doubt on the potential odd-parity superconductivity in this system [37,38], yet many other observations are still at odds with even parity superconductivity [39–42]. Thus, significant controversy remains. To study the electronic structure of S2RO4, calculations typically focus on individual two-dimensional RuO_2 sheets, which assume little or no interlayer interactions between the isolated sheets [43–48]. The validity of this assumption has not been experimentally tested in bulk due to the lack of Ruddlesden-Popper materials with varied separation between isolated RuO_2 sheets, i.e., RuO_2 layers that do not have a direct Ru-O-Ru bonding environment along the c-axis as in only Sr_2RuO_4. Along these lines, the synthesis of superlattices of $SrIrO_3$ and $SrTiO_3$, analogues to Sr_2IrO_4 and $Sr_3Ir_2O_7$, has shown unique dimensionality-controlled magnetic behavior [18–20]. Similar to these works, there has been a surge of interest in heterostructures of $SrRuO_3$ (SRO) inter-spaced with $SrTiO_3$ (STO) and other materials [49–64]. SRO is itself a ferromagnetic metal with many interesting behaviors in bulk and thin-film form [65–70]. In SL form, by increasing the relative thickness of the STO spacing layer, the coupling between the RuO_2 sheets can be directly manipulated. This has lead to many interesting discoveries including strong changes to magnetic anisotropy and moment [49,61]. However, the effect on the electronic configuration has not yet been fully explored in a series of SLs with systematic modulation of the confinement, which could perturb the dominant $d^5\underline{L}$, where $\underline{L}$ denotes a ligand hole on oxygen, state found from cluster calculations of bulk SRO [66,71–73]. Isolating the SRO layer in between inert STO layers, the SRO/STO

*Contact author: ujjal.lamichhane@okstate.edu

†Contact author: derek.meyers@okstate.edu

(SRSTO) SL is an ideal analogy for S2RO4 with varied coupling between RuO_2 sheets due to the dimensional confinement. The electronic structure of the SLs in comparison to S2RO4 is then of high importance in understanding and pursuing the analogy with the unconventional superconducting state. Moreover, since experiments on microscale pure S2RO4 crystal are still limited, [74] heterostructures like SRSTO SLs can be scaled to large-area films that may provide a practical foundation for the scalable ground state quantum computing technology if *p*-wave superconductivity can be stabilized [75,76].

In this paper, we report an electronic reconstruction derived from changing the RuO_2 confinement in ruthenate heterostructures. We synthesized SLs of SRO and STO on (001) STO substrates, i.e., one unit cell (uc) of SRO was layered with n unit cells (n = 1,2,3,4) of band insulating STO layers and the process was repeated 30 times to generate the [1SRO/nSTO] $\times$30 SRSTO heterostructures. The structural and electronic properties of the SLs and a reference SRO sample are then characterized using reflection high energy electron diffraction (RHEED), atomic force microscopy (AFM), X-Ray diffraction (XRD), synchrotron based resonant X-ray absorption spectroscopy (XAS), X-ray linear dichroism (XLD) and temperature-dependent resistivity, establishing the high structural and electronic quality of the materials. Anisotropic redistribution of charges between Ru and O orbitals and resultant changes to the expectation value of the angular portion of the spin-orbit coupling (SOC) are revealed by XAS and XLD. Density functional theory (DFT) calculations are used to confirm the minimal role of the Ti *d*-band doping in the observed changes. These findings demonstrate a novel pathway for the control of electronic structure in RuO_2 sheets without the use of doping which would destabilize any potential odd parity superconductivity that may arise.

II. EXPERIMENTAL METHODS

Epitaxial thin films of [1SRO/nSTO] $\times$ 30, n = 1,2,3,4 SLs were fabricated on (001) STO substrates by pulsed laser deposition (248 nm KrF excimer laser). SLs were synthesized at 700 °C substrate temperature under 100 mTorr oxygen partial pressure and laser fluence of 2 J/cm^2 with a repetition rate of 5 Hz for SRO and 2 Hz for STO. The laser spot was 0.024 cm^2 with a target-substrate distance of approximately 7.5 cm. The sample was annealed for 20 minutes and then cooled down slowly to room temperature in the presence of 200 Torr background oxygen pressure after the growth. The atomic scale precision of the *in-situ* growth was monitored using RHEED to ensure the proper unit cell layering of the SL. Single layer SRO films were grown with identical conditions. The surface morphology of the SLs was measured with AFM and the structural characterization was checked by high resolution x-ray diffraction (XRD) with Cu-$K_{\alpha 1}$ radiation (λ = 1.541838 Å) using a Bruker D8 Advance with a double bounce monochromator. Synchrotron-based XAS experiments at the Ru *L* edges were carried out at the beamline 4-ID-D and x-ray photoemission spectroscopy (XPS) measurements were collected at the beamline 29-ID of the Advanced Photon Source, Argonne National Laboratory.

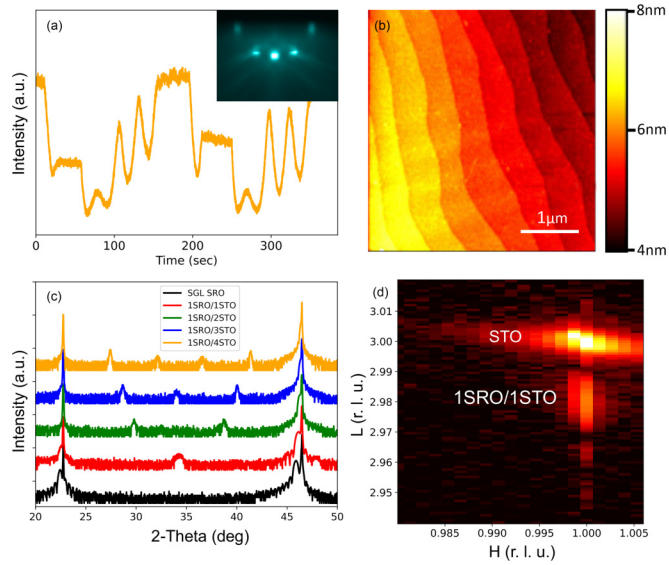

FIG. 1. (a) RHEED specular intensity taken during growth of 1SRO/4STO sample. The inset shows the post growth RHEED image of the same sample. (b) AFM image for 1SRO/1STO sample. (c) $2\theta - \omega$ XRD scan for 1SRO/nSTO SLs around the (002) Bragg peak. (d) RSM around the (103) Bragg peak of a 1SRO/1STO sample with substrate and sample labeled, features at lower L are thickness fringes.

Samples were measured at normal incidence, excepting the n = 4 SL which was measured 5° off the normal due to a nearby Bragg reflection. O *K* edge XAS and XLD, and Ti *L* edge XAS were performed at the 2-ID (SIX) beamline, NSLS-II, Brookhaven National Laboratory at 10° incidence angle.

The computational studies were performed with the SIESTA code [77,78] implementation of DFT [79,80]. We simulated the core and valence electrons with curated norm-conserving pseudopotentials obtained from the Pseudo-Dojo database [81], and used the generalized gradient approximation by Perdew Burke Ernzerhof [82] exchange correlation function. Our calculations were with the Hubbard-like term methodology of DFT + U [83], which can better account for the repulsion of the tightly bound 4*d* electrons of Ru. The self-consistent calculations were done with a grid equivalent to plane-wave cutoff energy of 365 Ry and with a Brillouin zone (BZ) sampling using Monkhorst-Pack grids [84] of 12 $\times$ 12$\times$ nz, where nz = 6, 4, 3, and 3 for each of the 1SRO/nSTO, n = 1, 2, 3, and 4 SLs. The calculations used the cell parameters found experimentally, $a = b$ = 3.905 Å, and c = 7.905, 11.849, 15.713, and 19.609 Å for each of the 1SRO/nSTO SLs. We calculated the optimal atomic positions by relaxing the structures using the conjugate gradient method until all atomic force components were less than 0.035 eV/Å.

III. RESULTS

The characteristic time dependent specular RHEED intensity oscillation of 1SRO/4STO is shown in Fig. 1(a). The diffraction pattern after the subsequent deposition of the SRO and STO layers signify the layer-by-layer growth whereas the

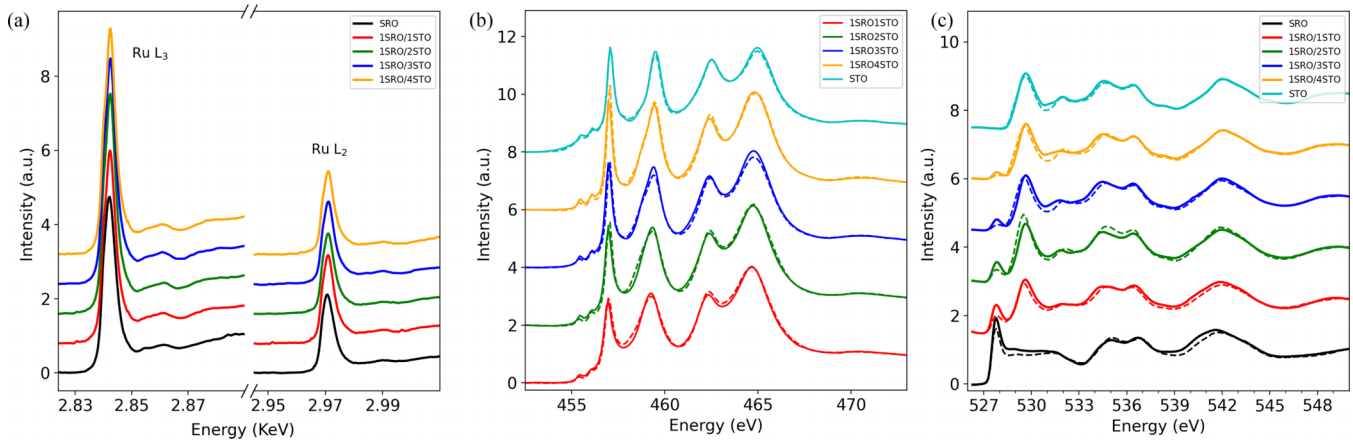

FIG. 2. (a) XAS data along Ru L_3 and L_2 edges. (b) Ti L edge XAS at 40 K temperature. (c) O K edge XAS at 40 K temperature. Solid (dashed) lines indicate in-plane (out-of-plane) polarization.

lack of significant damping of the intensity in the RHEED pattern confirms the high quality of the growing layers. Figure 1(a) inset RHEED image was recorded after annealing and cooling down the SL sample to room temperature. The specular and off specular Bragg reflections of the post growth films observed along the Laue circle with strongly developed Kikuchi lines demonstrate the excellent surface morphology. An AFM image with a field of view 4 μm × 4 μm in size of the 1SRO/1STO sample, as shown in Fig. 1(b), shows the high morphological quality of the film with atomic terraces observed after deposition. AFM images verify the uniform surface of the sample without any deviation from 2D growth. XRD gives further insight into the structural quality (periodicity and crystallinity) of the films. Figure 1(c) shows the $2\theta - \omega$ scans of all SLs (1SRO/nSTO, $n = 1,2,3,4$) and SRO thin films around the (002) Bragg peak using Cu-$K_{\alpha 1}$ focused radiation with a 4-circle diffractometer. This XRD image verifies the (002) peaks of all films are in good agreement with the Bragg peak. Also, the SLs peak at regular interval in this XRD scan confirms the number of STO layers in-between the SRO layers. Figure 1(d) shows a reciprocal space map (RSM) around the pseudocubic ($\bar{1}03$) Bragg peak, which confirms the film has the same in-plane lattice size as the substrate maintaining the epitaxy of the film.

We performed XAS measurements on the Ru $L_{3,2}$ edges in the total electron yield (TEY) mode to investigate the electronic and chemical structures of the films. Figure 2 shows the XAS spectra of a 12 nm SRO thin film reference and all SLs for the Ru L-, Ti L-, and O K-edges [(a)–(c), respectively]. The XAS spectra at the Ru L-edges (L_3 and L_2) have sharp atomic like white-line features which corresponds to $2p \rightarrow 4d$ electronic transition. The step-like edge features come from the $2p \rightarrow$ continuum electronic excitation and the fine structure oscillations are generated by the back scattering of photo-electrons of the neighboring atoms. The intensity of the L_3 absorption postedge is normalized to unity whereas the continuum step after the L_2 absorption edge is normalized to half [85]. This normalization corresponds to the initial core electron states at the L_3 and L_2 edges, i.e., the ratio of occupied $2p_{3/2}$ and $2p_{1/2}$ states. $2p_{3/2}$ has 4 electrons and $2p_{1/2}$ has 2 electrons. Ti L-edge XAS spectra in TEY mode for all SLs and STO substrate are shown in Fig. 2(b) with in-plane and nearly out-of-plane, 10° incidence (relative to the sample surface) linearly polarized light. The XAS spectra of all SLs are normalized to unity at the post edge after subtraction of the pre-edge intensity. This XAS is consistent with the Ti^{4+} XAS spectra found elsewhere in the literature [86–89], particularly with the absence of any features below 455 eV seen for Ti^{3+} and Ti^{2+} valences. However, as discussed below, there are some minor shifts of the e_g and t_{2g} features leading to small changes in the observed lineshapes. XPS further confirms the strong majority Ti^{4+} valence state (see Supplemental Material [90] and references therein [49,91–94]). Figure 2(c) shows the normalized XAS in TEY mode at the O K edge of the SLs performed at 40 K temperature with the same polarization plotting scheme as used for Ti. These XAS spectra clearly show the typical oxygen structure with a prepeak feature known to arise due to hybridization between the oxygen p-orbitals and the transition metal d-orbitals [95,96]. Unfortunately, O K edge XAS cannot distinguish between signal from the SRO, STO layers, or the STO substrate. However, the small penetration depth of the x-rays at this energy range (≈30 nm) combined with the small electron escape depth for TEY mode (≈1-10 nm) indicates the majority of the signal comes from the SL structure. The SL samples are all STO terminated, meaning the signal originating from the SRO layers will be progressively and nonlinearly suppressed depending on STO thickness. The prepeak feature around 527.75 eV is due to the presence of ligand hole states between the Ru 4d and O 2p orbitals, which only exist in the samples with SRO, confirming there is no ligand hole state in the STO layers between Ti and O. Features at higher energy are linked to oxygen hybridization with several Sr, Ti, and other Ru orbitals further from the Fermi level.

IV. DISCUSSION

A. Ru L-edge

The Ru L-edge absorption spectra contains direct information of the excited electronic structures of Ru 4d orbitals. Closer inspection of the L_3 and L_2 edges, Fig. 3(a), clearly indicates a significant change in the total spectral weight of the features as a function of STO layer thickness, despite the constant 1 unit cell thickness of SRO. Furthermore, dashed

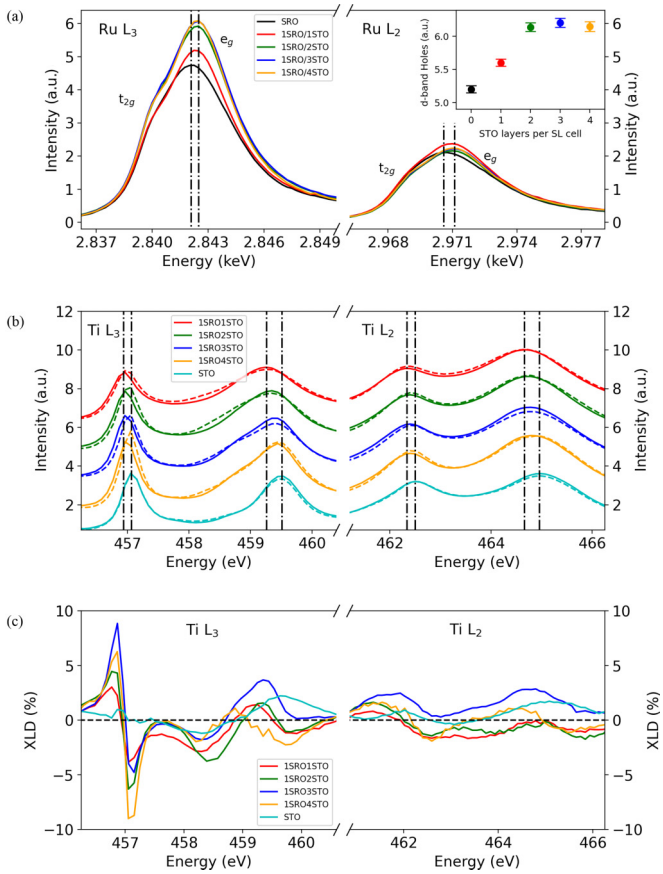

FIG. 3. (a) Ru L_3 and L_2 spectra. Vertical lines show approximate shift in peak energy between SRO and SLs. Inset shows relative number of holes relative to SRO based on integrated area of L_3 and L_2 spectra. (b) Ti L_3 and L_2 spectra with in-plane (solid) and out-of-plane (dashed) polarizations. (c) Ti L edge XLD (in-plane minus out-of-plane) at 40 K temperature.

lines highlight an observed shift of approximately 400 meV at both L_3 and L_2 edges in the SLs relative to the SRO film. Due to the two peak structure arising from the t_{2g} and e_g bands, labeled on the figure, and the inability to reliably separate their contributions, part of the peak shift may be due to the change in their respective spectral weights. Both of these observations indicate a change in the available states in the Ru d-band. Saturation effects, which can arise in TEY mode and distort the XAS lineshape, are not expected to be important here due to the normal incidence used, relatively high energy of the Ru L-edge, and the large change in intensity observed compared to prior findings for saturation effects in 3d oxide metals [97]. Here, the minimum absorption length at the Ru L_3 is estimated to be approximately two orders of magnitude larger than the electron escape depth, making saturation effects negligible. For our spectra, the increased spectral weight appears to be mostly in the e_g band. The sum of the areas of the L_3 and L_2 white lines after subtraction of the edge jump is used to calculate the relative number of available Ru 4d states in the heterostructures, using the SRO film as a reference for bulk like valence. The fitting of the L_3 spectra to calculate the area of white line features is shown in the Supplemental Material [90]. Figure 3(a) inset shows the calculated relative number of available states in the Ru $4d$ orbitals of SLs in reference to single layer SRO value of 5.2, as found via previously reported calculations, with the increased spectral weight percentage applied to find the new d-band hole count [66,71–73,98]. The increase in the relative number of available states in the heterostructures indicates either a strong change in the hybridized orbitals with O or electron doping into the Ti sites. We note PLD-grown SRO films are known to be slightly Ru deficient, amounting to less then a few percent difference from a 1:1 Ru/Sr ratio [99,100]. Such small changes in Ru concentration then cannot explain the large charge transfer observed here, nearly 1 electron, and any deficiency would be nearly constant due to identical growth conditions for all samples.

Thus, our data indicates the dominant $d^5\underline{L}$ state with 5.2 holes in the Ru d band for bulk-like SRO evolves to the d^4 state with around 6 holes for $n = 2, 3, 4$ SLs, lending support to the XAS analysis and prior calculations [66,71–73,101]. These studies showed the preferred Ru electron configuration in SRO and S2RO4 is either $t_{2g}^4 e_g^1$ or $t_{2g}^5 e_g^0$, with the ligand hole on oxygen. Upon increasing the STO layer thickness, our Ru L-edge data clearly shows an increase in available e_g states, implying the configuration evolves towards $t_{2g}^4 e_g^0$ with no oxygen ligand hole, with the increase in available states mostly in the e_g band. Thus, we find increasing 2D confinement moves the SRO out of the negative charge transfer regime. This interpretation rests on the assumption that the electron moves from the Ru d-band to the O p-band, filling the ligand hole state. A prior study also found small changes to the Ru XLD signal from t_{2g} orbital occupation changes, implying the energies of the t_{2g} orbitals are also altered with confinement [61].

It must be noted, the electron could, instead of filling the $\underline{L}$, move to the Ti d-band in the STO layers. Such interlayer charge transfer is a common finding in oxide heterostructures [94]. However, in this case no electron doping into the Ti states would be expected [94]. To experimentally confirm this scenario, results of Ti L-edge XAS and XLD are discussed next.

B. Ti L-edge

Closer inspection of the Ti L-edge XAS reveals more details of the spectra. Figure 3(b) shows a zoomed-in view of the Ti L_3 and L_2 absorption edges. For each edge there are two dominant features corresponding to the lower energy t_{2g} and e_g bands. Despite the nominal Ti^{4+} appearance, a gradual shifting of the peak positions as a function of STO thickness is apparent, as seen before [61]. Exact fitting of these features is not tenable due to the complex lineshapes, however rough estimates for total and relative peak shifts can be done. The vertical varied dashed lines indicate the approximate positions of the t_{2g} and e_g peaks for the two extreme end points, bulk STO and 1SRO/1STO SL, for both L_3 and L_2 edges. From this we find the t_{2g} band shifts down approximately 150 meV while the e_g band shifts down by approximately 275 meV. The approximately 125 meV of relative energy shift between the t_{2g} and e_g features indicates a small systematic decrease in the crystal field splitting as a function of decreasing STO weight in the SL cell. The 150 meV total shift of both features could indicate a small, but non-zero charge transfer into the

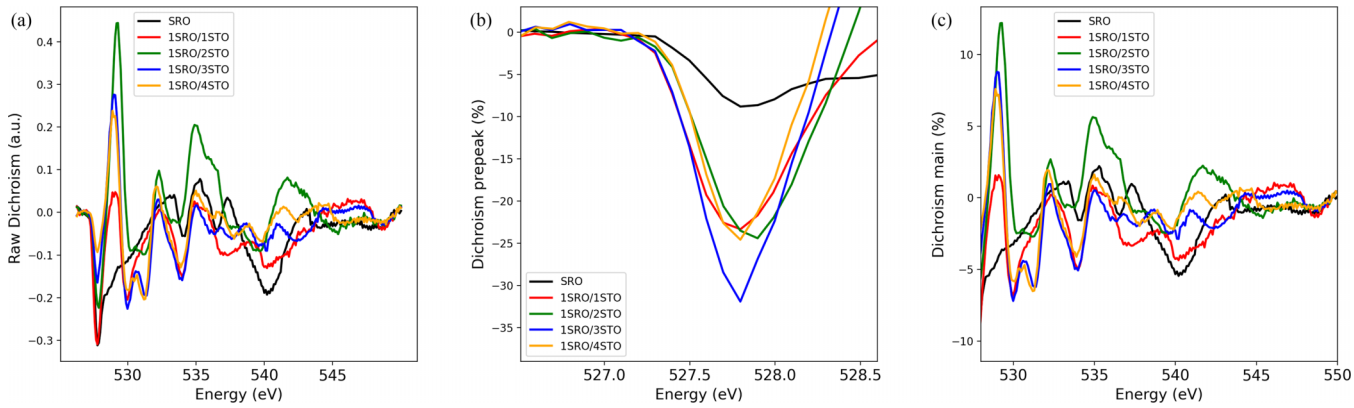

FIG. 4. (a) Raw XLD data. (b) XLD normalized to the prepeak total spectral weight. (c) XLD normalized to the white line feature total spectral weight. All data from the O K-edge.

Ti d-band and/or changes with the O hybridization at the interface with SRO.

These findings are further supported by Ti XLD results, Fig. 3(c). XLD is calculated by subtracting the normalized out-of-plane polarized spectra from the normalized in-plane polarized spectra. The subtraction of these two spectra gives information on the orientation of the unoccupied orbitals. The sample was in grazing incidence such that linear vertical polarization is along the in-plane direction of the sample whereas linear horizontal polarization is 10° off out of plane. For the L_3 edge, an increased dichroism for the t_{2g} band is observed for the SL samples relative to the STO substrate reference. We note the systematics are unclear likely due to low point density and competing effects, such as a combination of changing interfacial spectral weight due to the shallow electron escape depth and the changing proportion of interfacial vs bulk-like STO. Overall, the Ti L_3 data shows a strong relative shift of the energies of in-plane vs out-of-plane orbitals in the SL samples vs the bulk STO, pointing to the interfacial reconstruction as a likely culprit for the observed changes in Ti. The small observed doping cannot account for the nearly one entire electron charge transfer deciphered from the Ru L-edge data, pointing to oxygen as the likely majority recipient.

C. O K-edge

The O K-edge data, Fig. 2(c), is quite complex due to the strong hybridization of O with the Ti, Ru, and Sr orbitals. The well-known pre-peak feature around 527.75 eV derives from hybridization of O p and Ru d orbitals, and is absent in pure STO XAS. The data is normalized by subtraction of the pre-edge intensity and then division by the post-edge intensity to give a total edge jump of unity. However, direct comparison of the prepeak and other features between samples is hindered by the changing proportion of the SRO relative to STO layers as discussed earlier. Due to the use of TEY mode, the electron escape depth also strongly favors the top most layers meaning the relative strength of the pre-peak feature with respect to the entire spectra is not readily decipherable. Despite this, the strong reduction in pre-peak weight appears inconsistent with the fraction of the signal coming from the SRO layers due to the changes in STO top layer thickness, with the $n = 4$ SL showing a much weaker pre-peak compared to the $n = 1$ SL for instance. This implies at least some of the reduction in spectral weight comes from reduction of the ligand hole state on oxygen.

To gain more insight into the electronic structure around oxygen, we utilized XLD for the investigation of O $2p$ orbital hybridization, Figs. 4(a)–4(c). These measurements were done in the same geometry as described above for Ti L-edge XLD. Figure 4(a) shows the raw subtracted data. Normalization of this data is then a particular challenge due to the changing contribution of the SRO layers to the overall spectra. To address this, we display different regions of the XLD in Figs. 4(b) and 4(c) with normalization done by dividing by the total pre-peak intensity at approximately 527.75 eV and by dividing by the maximum of the white line feature XLD at around 529 eV, respectively. This procedure then ensures the pre-peak XLD percentage represents the relative difference in orbital occupation of in-plane vs out-of-plane for hybridized Ru-O orbitals, while the remaining spectrum XLD percentage is more accurate for the Ti-O and Sr-O hybridization.

For the pre-peak feature, it is immediately clear that the hybridized Ru $4d$ and O $2p$ orbitals gain a strong occupation orientation dependence not present in bulk-like SRO, with a significant 25-30% XLD signal, compared to an approximately 5-10% signal for bulk-like SRO as seen in prior work being highly thickness dependent [102]. This implies a significant electronic reconstruction occurs in all SL samples with the hybridized O $2p$ - Ru $4d$ orbitals. The large negative signal for the hybridized Ru $4d$ orbitals in the XLD indicate the availability of more electron states for Ru nearly out of plane polarization, i.e., along the c-axis rather than in the a-b plane. This means there are far fewer in-plane available electron states (hybridized $p_{x,y}$) than out-of-plane states for the SL (hybridied p_z).

D. Electronic reconstruction

Taken together, the observation of increasing available states at the Ru edge in concert with the relative decrease in the available in-plane hybridized states with O implies an anisotropic reconstruction of the ligand hole state as a function of interlayer coupling. Similar changes to the hybridized orbitals for artificial heterostructures have been observed previously in nickelate heterostructures [103]. In the case of

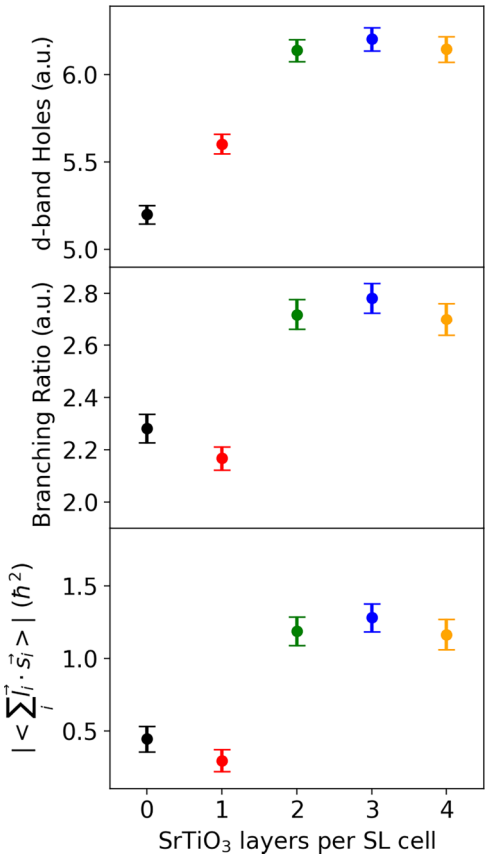

FIG. 5. Top panel: d-band holes based on prior cluster calculation findings and relative spectral weight. Middle panel: Branching ratio defined as ratio of the spectral weight of the L_3 and L_2 resonant features after edge jump substraction. Bottom panel: Magnitude of the $\langle \sum_i \vec{l}_i \cdot \vec{s}_i \rangle$ calculated from hole number and BR.

SRO, it was previously found that the system is majority $d^5\underline{L}$ with a smaller proportion of the nominal d^4 state, giving a total d-hole count of $n_h = 5.2$ via cluster calculations and valence transition models [66,71–73].

The increasing confinement of the active RuO_2 layers as a function of STO thickness then appears to directly manipulate the electronic structure, changing the relative occupation of the Ru t_{2g} and e_g orbitals. It is likely such behavior is linked to the decreasing electronic bandwidth with STO thickness, as evidenced by the transport behavior, leading to localized states and more isotropic Ru electron distribution [90]. Such findings have important implications for studies on potential superconductivity in SRO heterostructures, where the confinement of RuO_2 layers, mediated by a direct O-Ti-O c-axis coupling, is not directly comparable to the RuO_2 sheets in S2RO4, where the apical oxygens do not directly bond with the apical oxygens of the following RuO_2 layers.

Figure 5(a) shows the change in total integrated area of the Ru L_3 and L_2 XAS features, which indicates the number of holes (available states) in the Ruthenium d-band, as previously shown in Fig. 3(a) inset. The relative spectral weight of these features is known as the branching ratio (BR) and is sensitive to both the available holes and the angular part of the SOC of the Ru states, Fig. 5(b) [104–107]. Deviations of the BR from the statistical value of 2 indicate stronger SOC. A prior report found that strain induced by SRO growth on STO leads to an increase of the BR to around 2.2 [66]. Here they found the applied strain acts to dequench the orbital moment of the SRO leading to the increased BR. In our case, the SRO film and $n = 1$ SL are both within error of this value, implying similar dequenching effects. However, the $n = 2, 3, 4$ SLs all show a much larger BR of approximately 2.7, implying a strong increase in effective SOC. Interestingly, in the prior work a similar value to 2.7 was found for SRO on LSAT substrates, which was attributed to the higher epitaxial strain enhancing the dequenching effect [66]. However, for our SLs the strain is not varied implying a different source. The significant increase is then likely due to the changing d-electron configuration. The dominant $d^5\underline{L}$ state leading to the 5.2 hole count is replaced by a majority d^4 character leading to the approximately 6 hole count in the $n = 2, 3, 4$ SLs.

The spin-obit coupling ground state expectation value, $\langle \sum_i \vec{l}_i \cdot \vec{s}_i \rangle$ can be calculated as $\langle \sum_i \vec{l}_i \cdot \vec{s}_i \rangle = n_h \frac{BR-2}{BR+1}$, where n_h is the number of holes in the $4d$ band [107]. Using this equation combined with the data in Figs. 5(a) and 5(b) we extract the magnitude of $\langle \sum_i \vec{l}_i \cdot \vec{s}_i \rangle$ for each sample, Fig. 5(c). For the SRO film and $n = 1$ SL the expectation value is around $0.4\hbar^2$. Compared to the fully quenched case in bulk SRO giving $\langle \sum_i \vec{l}_i \cdot \vec{s}_i \rangle = 0$, this values implies a larger SOC due to the orbital de-quenching. For the $n = 2, 3, 4$ SLs, this value is increased to approximately $1.2\hbar^2$, giving much larger SOC interaction in these systems. This result is surprising, as the $d^5(t_{2g}^4 e_g^1)\underline{L}$ configuration should have a higher S value than the $d^4(t_{2g}^4 e_g^0)$ state [101]. However, the $d^5(t_{2g}^5 e_g^0)\underline{L}$ would have a lower S-value which better agrees with these results, but cannot explain the observed primary change in the spectral weight observed at the e_g feature, Fig. 3(a) [66,71–73]. With the constant small strain value across our samples, this implies the confinement also plays a strong role in orbital moment de-quenching, comparable to the effect of larger strain values [66]. Such significant dequenching of the orbital moment is achieved here by the changes to the local crystal field effect due to the heterostructuring. These observations cumulatively point to confinement-driven electron configuration changes as an important factor for the observed increases in magnetic anisotropy and moment previously found in ruthenate SL materials [49,54,61,66,72,73]. The effect of octahedral rotation and tilting due to the structural changes likely plays a role as well in driving the observed changes in hybridization, as the c^- octahedral rotation was found to vary strongly for these SLs leading to lifting the degeneracy of the t_{2g} orbitals [61].

Recent theoretical work on superconducting S2RO4 using a valence transition model also showed the $d^5\underline{L}$ state can explain some of the unusual properties of the system, with a significant role of the oxygen ligand hole [73]. This study followed from work using the same modeling on cuprates [108]. In the context of our results, these works confirm the SL samples present an excellent analogy to the S2RO4 system, with the advantage of tuning the balance of the $d^5\underline{L}$ and d^4 states via confinement. Doping within the STO layers to avoid scattering defects in the RuO_2 sheets may then allow further control of these states towards stabilizing SC in these artificial systems.

V. CONCLUSION

We synthesized high-quality epitaxial 1SRO/nSTO superlattices via pulsed laser deposition on (001) STO substrates. The combination of several characterization tools including RHEED, AFM, XRD, RSM, XAS, and XLD revealed the excellent structural, chemical, and electronic quality of the heterostructures. XAS at Ru, Ti, and O edges confirm an electronic reconstruction derived from the confinement of RuO_2 plane in SRO/STO heterostructures. The SRO thin film shows bulk-like dominant $d^5\underline{L}$ configuration while the SLs show a progression to the d^4 state which saturates for $n = 2, 3, 4$ SLs. XLD data supports this finding showing a distinct deviation from the more isotropic occupation of the hybridized Ru $4d$ and O $2p$ orbitals seen in bulk-like SRO due to 2D confinement. The lack of significant doping of the Ti is supported by XAS measurements and DFT calculations, which find a dominant Ti^{4+} valence and changes to the crystal field splitting as a function of STO thickness. Future work on the magnetic behavior and the complete band structure of the heterostructures can be done to compare with the electronic band structure of the superconducting S2RO4 to further the analogy to the bulk unconventional superconducting material.

ACKNOWLEDGMENTS

We would like to acknowledge support provided by Oklahoma State University in the form of startup funding for D.M. D.M. was also partially supported by the National Science Foundation under Grant No. DMR-2340300. The XAS measurements at the Advanced Photon Source were supported in part by the U.S. Department of Energy, Office of Science, Basic Energy Sciences, Materials Science and Engineering Division. This research used resources of the Advanced Photon Source, a U.S. Department of Energy (DOE) Office of Science User Facility operated for the DOE Office of Science by Argonne National Laboratory under Contract No. DE-AC02-06CH11357. This research used beam line 2-ID of the National Synchrotron Light Source II, a U.S. DOE Office of Science User Facility operated for the DOE Office of Science by Brookhaven National Laboratory under Contract No. DESC0012704. Calculations were performed at the High Performance Computing Center at Oklahoma State University supported in part through the National Science Foundation Grant No. OAC-1531128. Parts of this work were carried out in the Microscopy Laboratory, Oklahoma State University, which received funds for purchasing the equipment from the NSF MRI program.

[1] P. A. Lee, N. Nagaosa, and X.-G. Wen, Doping a Mott insulator: Physics of high-temperature superconductivity, Rev. Mod. Phys. **78**, 17 (2006).

[2] M. Imada, A. Fujimori, and Y. Tokura, Metal-insulator transitions, Rev. Mod. Phys. **70**, 1039 (1998).

[3] B. Keimer and J. Moore, The physics of quantum materials, Nat. Phys. **13**, 1045 (2017).

[4] M. Liu, H. Y. Hwang, H. Tao, A. C. Strikwerda, K. Fan, G. R. Keiser, A. J. Sternbach, K. G. West, S. Kittiwatanakul, J. Lu *et al.*, Terahertz-field-induced insulator-to-metal transition in vanadium dioxide metamaterial, Nature (London) **487**, 345 (2012).

[5] J. Chakhalian, J. W. Freeland, G. Srajer, J. Strempfer, G. Khaliullin, J. C. Cezar, T. Charlton, R. Dalgliesh, C. Bernhard, G. Cristiani *et al.*, Magnetism at the interface between ferromagnetic and superconducting oxides, Nat. Phys. **2**, 244 (2006).

[6] Y. Tokura, Critical features of colossal magnetoresistive manganites, Rep. Prog. Phys. **69**, 797 (2006).

[7] L. Hao, D. Meyers, C. Frederick, G. Fabbris, J. Yang, N. Traynor, L. Horak, D. Kriegner, Y. Choi, J.-W. Kim *et al.*, Two-dimensional $J_{\text{eff}} = 1/2$ antiferromagnetic insulator unraveled from interlayer exchange coupling in artificial perovskite iridate superlattices, Phys. Rev. Lett. **119**, 027204 (2017).

[8] J. Yang, L. Hao, D. Meyers, T. Dasa, L. Xu, L. Horak, P. Shafer, E. Arenholz, G. Fabbris, Y. Choi *et al.*, Strain-modulated Slater-Mott crossover of pseudospin-half square-lattice in $(SrIrO_3)_1/(SrTiO_3)_1$ superlattices, Phys. Rev. Lett. **124**, 177601 (2020).

[9] J. Hwang, J. Y. Zhang, J. Son, and S. Stemmer, Nanoscale quantification of octahedral tilts in perovskite films, Appl. Phys. Lett. **100**, 191909 (2012).

[10] J. He, A. Borisevich, S. V. Kalinin, S. J. Pennycook, and S. T. Pantelides, Control of octahedral tilts and magnetic properties of perovskite oxide heterostructures by substrate symmetry, Phys. Rev. Lett. **105**, 227203 (2010).

[11] H. Rotella, U. Lüders, P.-E. Janolin, V. H. Dao, D. Chateigner, R. Feyerherm, E. Dudzik, and W. Prellier, Octahedral tilting in strained $LaVO_3$ thin films, Phys. Rev. B **85**, 184101 (2012).

[12] J. Chakhalian, A. J. Millis, and J. Rondinelli, Whither the oxide interface, Nat. Mater. **11**, 92 (2012).

[13] H. Y. Hwang, Y. Iwasa, M. Kawasaki, B. Keimer, N. Nagaosa, and Y. Tokura, Emergent phenomena at oxide interfaces, Nat. Mater. **11**, 103 (2012).

[14] S. G. Jeong, H. Kim, S. J. Hong, D. Suh, and W. S. Choi, Symmetry-driven spin-wave gap modulation in nanolayered $SrRuO_3/SrTiO_3$ heterostructures: Implications for spintronic applications, ACS Appl. Nano Mater. **4**, 2160 (2021).

[15] S. W. Cho, S. G. Jeong, H. Y. Kwon, S. Song, S. Han, J. H. Han, S. Park, W. S. Choi, S. Lee, and J. W. Choi, Tailoring topological Hall effect in $SrRuO_3/SrTiO_3$ superlattices, Acta Mater. **216**, 117153 (2021).

[16] A. S. Goossens, M. Leiviskä, and T. Banerjee, Anisotropy and current control of magnetization in $SrRuO_3/SrTiO_3$ heterostructures for spin-memristors, Front. Nanotechnol. **3**, 680468 (2021).

[17] J. Matsuno, K. Ihara, S. Yamamura, H. Wadati, K. Ishii, V. V. Shankar, H.-Y. Kee, and H. Takagi, Engineering a spin-orbital magnetic insulator by tailoring superlattices, Phys. Rev. Lett. **114**, 247209 (2015).

[18] L. Hao, D. Meyers, H. Suwa, J. Yang, C. Frederick, T. R. Dasa, G. Fabbris, L. Horak, D. Kriegner, Y. Choi *et al.*, Giant magnetic response of a two-dimensional antiferromagnet, Nat. Phys. **14**, 806 (2018).

[19] D. Meyers, K. Nakatsukasa, S. Mu, L. Hao, J. Yang, Y. Cao, G. Fabbris, H. Miao, J. Pelliciari, D. McNally *et al.*, Decoupling carrier concentration and electron-phonon coupling in oxide heterostructures observed with resonant inelastic x-ray scattering, Phys. Rev. Lett. **121**, 236802 (2018).

[20] D. Meyers, Y. Cao, G. Fabbris, N. J. Robinson, L. Hao, C. Frederick, N. Traynor, J. Yang, J. Lin, M. Upton *et al.*, Magnetism in iridate heterostructures leveraged by structural distortions, Sci. Rep. **9**, 4263 (2019).

[21] B. R. Sankhi, U. Lamichhane, S. Mandal, R. Sachan, E. Turgut, and D. Meyers, Interface effects on magnetic anisotropy and domain wall depinning fields in $Pt/Co/AlO_x$ thin films, Magnetochemistry **8**, 154 (2022).

[22] M. Izumi, K. Nakazawa, and Y. Bando, T_c suppression of $SrRuO_3/SrTiO_3$ superlattices, J. Phys. Soc. Jpn. **67**, 651 (1998).

[23] M. Kawasaki, M. Izumi, Y. Konishi, T. Manako, and Y. Tokura, Perfect epitaxy of perovskite manganite for oxide spin-electronics, Mater. Sci. Eng.: B **63**, 49 (1999).

[24] I. H. Choi, S. G. Jeong, T. Min, J. Lee, W. S. Choi, and J. S. Lee, Giant enhancement of electron–phonon coupling in dimensionality-controlled $SrRuO_3$ heterostructures, Adv. Sci. **10**, 2300012 (2023).

[25] J. Mun, E. K. Ko, B. Kang, B. Gil, C. H. Kim, S. Hahn, J. Song, Y. Zhu, C. Sohn, T. W. Noh *et al.*, Extended oxygen octahedral tilt proximity near oxide heterostructures, Nano Lett. **23**, 1036 (2023).

[26] K. Eom, M. Yu, J. Seo, D. Yang, H. Lee, J.-W. Lee, P. Irvin, S. H. Oh, J. Levy, and C.-B. Eom, Electronically reconfigurable complex oxide heterostructure freestanding membranes, Sci. Adv. **7**, eabh1284 (2021).

[27] Z. Deng, J. Liu, Y. Hong, L. Wei, S. Hu, W. Xiao, L. Li, L. Wang, K. Chen, and Z. Liao, Quasi-two-dimensional ferromagnetic $SrRuO_3$ grown by pulsed laser deposition with layer-by-layer growth fashion, Adv. Mater. Interfaces **9**, 2201371 (2022).

[28] M. Kim, C.-J. Kang, J.-H. Han, K. Kim, and B. Kim, Tunable electronic and magnetic phases in layered ruthenates: Strained $SrRuO_3/SrTiO_3$ heterostructures, Phys. Rev. B **106**, L201103 (2022).

[29] T.-Z. Wang, J. Xia, R. Yang, and X. Miao, Stable retention in $SrTiO_3/SrRuO_3$ heterostructure-based memristive devices, Sci. China Mater. **66**, 1140 (2023).

[30] P. Siwakoti, Z. Wang, M. Saghayezhian, D. Howe, Z. Ali, Y. Zhu, and J. Zhang, Abrupt orthorhombic relaxation in compressively strained ultrathin $SrRu\,O_3$ films, Phys. Rev. Mater. **5**, 114409 (2021).

[31] Y. Maeno, H. Hashimoto, K. Yoshida, S. Nishizaki, T. Fujita, J. Bednorz, and F. Lichtenberg, Superconductivity in a layered perovskite without copper, Nature (London) **372**, 532 (1994).

[32] T. Rice and M. Sigrist, Sr_2RuO_4: An electronic analogue of 3He? J. Phys.: Condens. Matter **7**, L643 (1995).

[33] A. P. Mackenzie and Y. Maeno, The superconductivity of Sr_2RuO_4 and the physics of spin-triplet pairing, Rev. Mod. Phys. **75**, 657 (2003).

[34] C. Kallin, Chiral p-wave order in Sr_2RuO_4, Rep. Prog. Phys. **75**, 042501 (2012).

[35] A. P. Mackenzie, T. Scaffidi, C. W. Hicks, and Y. Maeno, Even odder after twenty-three years: The superconducting order parameter puzzle of Sr_2RuO_4, npj Quantum Mater. **2**, 40 (2017).

[36] A. Mackenzie, A personal perspective on the unconventional superconductivity of Sr_2RuO_4, J. Supercond. Novel Magn. **33**, 177 (2020).

[37] K. Ishida, M. Manago, K. Kinjo, and Y. Maeno, Reduction of the ^{17}O Knight shift in the superconducting state and the heat-up effect by NMR pulses on Sr_2RuO_4, J. Phys. Soc. Jpn. **89**, 034712 (2020).

[38] A. Pustogow, Y. Luo, A. Chronister, Y.-S. Su, D. Sokolov, F. Jerzembeck, A. P. Mackenzie, C. W. Hicks, N. Kikugawa, S. Raghu *et al.*, Constraints on the superconducting order parameter in Sr_2RuO_4 from oxygen-17 nuclear magnetic resonance, Nature (London) **574**, 72 (2019).

[39] E. Pavarini and I. I. Mazin, First-principles study of spin-orbit effects and NMR in Sr_2RuO_4, Phys. Rev. B **74**, 035115 (2006).

[40] M. W. Haverkort, I. S. Elfimov, L. H. Tjeng, G. A. Sawatzky, and A. Damascelli, Strong spin-orbit coupling effects on the Fermi surface of Sr_2RuO_4 and Sr_2RhO_4, Phys. Rev. Lett. **101**, 026406 (2008).

[41] E. J. Rozbicki, J. F. Annett, J.-R. Souquet, and A. P. Mackenzie, Spin–orbit coupling and k-dependent Zeeman splitting in strontium ruthenate, J. Phys.: Condens. Matter **23**, 094201 (2011).

[42] C. N. Veenstra, Z.-H. Zhu, M. Raichle, B. M. Ludbrook, A. Nicolaou, B. Slomski, G. Landolt, S. Kittaka, Y. Maeno, J. H. Dil, I. S. Elfimov, M. W. Haverkort, and A. Damascelli, Spin-orbital entanglement and the breakdown of singlets and triplets in Sr_2RuO_4 revealed by spin-and angle-resolved photoemission spectroscopy, Phys. Rev. Lett. **112**, 127002 (2014).

[43] T. Oguchi, Electronic band structure of the superconductor Sr_2RuO_4, Phys. Rev. B **51**, 1385 (1995).

[44] V. Zabolotnyy, D. Evtushinsky, A. Kordyuk, T. Kim, E. Carleschi, B. Doyle, R. Fittipaldi, M. Cuoco, A. Vecchione, and S. Borisenko, Renormalized band structure of Sr_2RuO_4: A quasiparticle tight-binding approach, J. Electron Spectrosc. Relat. Phenom. **191**, 48 (2013).

[45] S. Acharya, D. Pashov, E. Chachkarova, M. v. Schilfgaarde, and C. Weber, Electronic structure correspondence of singlet-triplet scale separation in strained Sr_2RuO_4, Appl. Sci. **11**, 508 (2021).

[46] E. Z. Kurmaev, S. Stadler, D. L. Ederer, Y. Harada, S. Shin, M. M. Grush, T. A. Callcott, R. C. C. Perera, D. A. Zatsepin, N. Ovechkina, M. Kasai, Y. Tokura, T. Takahashi, K. Chandrasekaran, R. Vijayaraghavan, and U. V. Varadaraju, Electronic structure of Sr_2RuO_4: X-ray fluorescence emission study, Phys. Rev. B **57**, 1558 (1998).

[47] Z. Ropka, R. Radwański, and A. Baran, Electronic structure and magnetism of Sr_2RuO_4, Physica C: Superconductivity **387**, 262 (2003).

[48] K. K. Ng and M. Sigrist, The role of spin-orbit coupling for the superconducting state in Sr_2RuO_4, Europhys. Lett. **49**, 473 (2000).

[49] H. Boschker, T. Harada, T. Asaba, R. Ashoori, A. V. Boris, H. Hilgenkamp, C. R. Hughes, M. E. Holtz, L. Li, D. A. Muller, H. Nair, P. Reith, X. Renshaw Wang, D. G. Schlom, A. Soukiassian, and J. Mannhart, Ferromagnetism and conductivity in atomically thin $SrRuO_3$, Phys. Rev. X **9**, 011027 (2019).

[50] S. J. Callori, J. Gabel, D. Su, J. Sinsheimer, M. V. Fernandez-Serra, and M. Dawber, Ferroelectric $PbTiO_3/SrRuO_3$

superlattices with broken inversion symmetry, Phys. Rev. Lett. **109**, 067601 (2012).

[51] X. Niu, B.-B. Chen, N. Zhong, P.-H. Xiang, and C.-G. Duan, Topological Hall effect in $SrRuO_3$ thin films and heterostructures, J. Phys.: Condens. Matter **34**, 244001 (2022).

[52] S. G. Jeong, J. Kim, A. Seo, S. Park, H. Y. Jeong, Y.-M. Kim, V. Lauter, T. Egami, J. H. Han, and W. S. Choi, Unconventional interlayer exchange coupling via chiral phonons in synthetic magnetic oxide heterostructures, Sci. Adv. **8**, eabm4005 (2022).

[53] Y. Gu, Q. Wang, W. Hu, W. Liu, Z. Zhang, F. Pan, and C. Song, An overview of $SrRuO_3$-based heterostructures for spintronic and topological phenomena, J. Phys. D **55**, 233001 (2022).

[54] Z. Cui, Y. Zhang, X. Zhai, H. Chen, Y.-D. Chuang, J. Guo, Z. Fu, Z. Li, and Y. Lu, Interface engineering of phase separation in $SrRuO_3/SrTiO_3$ hybrid superlattices, Phys. Rev. B **106**, 024424 (2022).

[55] G. Herranz, B. Martínez, J. Fontcuberta, F. Sánchez, M. V. Garcıa-Cuenca, C. Ferrater, and M. Varela, $SrRuO_3/SrTiO_3/SrRuO_3$ heterostructures for magnetic tunnel junctions, J. Appl. Phys. **93**, 8035 (2003).

[56] M. Saghayezhian, Z. Wang, D. Howe, P. Siwakoti, E. Plummer, Y. Zhu, and J. Zhang, Formation of dislocations via misfit strain across interfaces in epitaxial $BaTiO_3$ and $SrIrO_3$ heterostructures, J. Phys.: Condens. Matter **33**, 275003 (2021).

[57] P. Roy, D. Zhang, A. R. Mazza, N. Cucciniello, S. Kunwar, H. Zeng, A. Chen, and Q. Jia, Manipulating topological Hall-like signatures by interface engineering in epitaxial ruthenate/manganite heterostructures, Nanoscale **15**, 17589 (2023).

[58] R. Tanguturi and A. Nande, Interface engineering in oxide heterostructures for novel magnetic and electronic properties, in *Functional Materials from Carbon, Inorganic, and Organic Sources* (Woodhead Publishing, Sawston, UK, 2023), pp. 245–269.

[59] W. Zheng, Y. Wang, C. Jin, R. Yin, D. Li, P. Wang, S. Liu, X. Wang, D. Zheng, and H. Bai, Ferroelectric resistance switching in $Pt/Fe/BiFeO_3/SrRuO_3/SrTiO_3$ heterostructures, Phys. Chem. Chem. Phys. **22**, 13277 (2020).

[60] N. Strkalj, G. De Luca, M. Campanini, S. Pal, J. Schaab, C. Gattinoni, N. A. Spaldin, M. D. Rossell, M. Fiebig, and M. Trassin, Depolarizing-field effects in epitaxial capacitor heterostructures, Phys. Rev. Lett. **123**, 147601 (2019).

[61] Z. Cui, A. J. Grutter, H. Zhou, H. Cao, Y. Dong, D. A. Gilbert, J. Wang, Y.-S. Liu, J. Ma, Z. Hu *et al.*, Correlation-driven eightfold magnetic anisotropy in a two-dimensional oxide monolayer, Sci. Adv. **6**, eaay0114 (2020).

[62] S. G. Jeong, J. Y. Oh, L. Hao, J. Liu, and W. S. Choi, Correlated quantum phenomena of spin–orbit coupled perovskite oxide heterostructures: Cases of $SrRuO_3$ and $SrIrO_3$ based artificial superlattices, Adv. Funct. Mater. **33**, 2301770 (2023).

[63] S. G. Jeong, G. Han, S. Song, T. Min, A. Y. Mohamed, S. Park, J. Lee, H. Y. Jeong, Y.-M. Kim, D.-Y. Cho *et al.*, Propagation control of octahedral tilt in $SrRuO_3$ via artificial heterostructuring, Adv. Sci. **7**, 2001643 (2020).

[64] J. Zhang, L. Cheng, H. Cao, M. Bao, J. Zhao, X. Liu, A. Zhao, Y. Choi, H. Zhou, P. Shafer *et al.*, The exceedingly strong two-dimensional ferromagnetism in bi-atomic layer $SrRuO_3$ with a critical conduction transition, Nano Res. **15**, 7584 (2022).

[65] H. T. Dang, J. Mravlje, A. Georges, and A. J. Millis, Electronic correlations, magnetism, and Hund's rule coupling in the ruthenium perovskites $SrRuO_3$ and $CaRuO_3$, Phys. Rev. B **91**, 195149 (2015).

[66] S. Tyagi, V. Sathe, G. Sharma, D. Phase, and V. Reddy, Strain healing of spin–orbit coupling: A cause for enhanced magnetic moment in epitaxial $SrRuO_3$ thin films, J. Phys.: Condens. Matter **32**, 305501 (2020).

[67] K. Maiti and R. S. Singh, Evidence against strong correlation in 4*d* transition-metal oxides $CaRuO_3$ and $SrRuO_3$, Phys. Rev. B **71**, 161102(R) (2005).

[68] D. Kan, R. Aso, R. Sato, M. Haruta, H. Kurata, and Y. Shimakawa, Tuning magnetic anisotropy by interfacially engineering the oxygen coordination environment in a transition metal oxide, Nat. Mater. **15**, 432 (2016).

[69] N. J. Schreiber, L. Miao, H. P. Nair, J. P. Ruf, L. Bhatt, Y. A. Birkholzer, G. N. Kotsonis, L. F. Kourkoutis, K. M. Shen, and D. G. Schlom, Enhanced T_C in $SrRuO_3/DyScO_3$ (110) thin films with high residual resistivity ratio, APL Mater. **11**, 111101 (2023).

[70] D. Kan and Y. Shimakawa, Strain effect on structural transition in $SrRuO_3$ epitaxial thin films, Cryst. Growth Des. **11**, 5483 (2011).

[71] E. B. Guedes, M. Abbate, K. Ishigami, A. Fujimori, K. Yoshimatsu, H. Kumigashira, M. Oshima, F. C. Vicentin, P. T. Fonseca, and R. J. O. Mossanek, Core level and valence band spectroscopy of $SrRuO_3$: Electron correlation and covalence effects, Phys. Rev. B **86**, 235127 (2012).

[72] S. Agrestini, Z. Hu, C.-Y. Kuo, M. W. Haverkort, K.-T. Ko, N. Hollmann, Q. Liu, E. Pellegrin, M. Valvidares, J. Herrero-Martin, P. Gargiani, P. Gegenwart, M. Schneider, S. Esser, A. Tanaka, A. C. Komarek, and L. H. Tjeng, Electronic and spin states of $SrRuO_3$ thin films: An x-ray magnetic circular dichroism study, Phys. Rev. B **91**, 075127 (2015).

[73] S. Mazumdar, Negative charge-transfer gap and even parity superconductivity in Sr_2RuO_4, Phys. Rev. Res. **2**, 023382 (2020).

[74] H. Nobukane, K. Inagaki, K. Ichimura, K. Yamaya, S. Takayanagi, I. Kawasaki, K. Tenya, H. Amitsuka, K. Konno, Y. Asano *et al.*, Parity violation in a single domain of spin-triplet Sr_2RuO_4 superconductors, Solid State Commun. **149**, 1212 (2009).

[75] B. van Heck, A. Akhmerov, F. Hassler, M. Burrello, and C. Beenakker, Coulomb-assisted braiding of Majorana fermions in a Josephson junction array, New J. Phys. **14**, 035019 (2012).

[76] T. Hyart, B. van Heck, I. C. Fulga, M. Burrello, A. R. Akhmerov, and C. W. J. Beenakker, Flux-controlled quantum computation with Majorana fermions, Phys. Rev. B **88**, 035121 (2013).

[77] A. García, N. Papior, A. Akhtar, E. Artacho, V. Blum, E. Bosoni, P. Brandimarte, M. Brandbyge, J. I. Cerdá, F. Corsetti *et al.*, SIESTA: Recent developments and applications, J. Chem. Phys. **152**, 204108 (2020).

[78] J. M. Soler, E. Artacho, J. D. Gale, A. García, J. Junquera, P. Ordejón, and D. Sánchez-Portal, The SIESTA method for *ab initio* order-*N* materials simulation, J. Phys.: Condens. Matter **14**, 2745 (2002).

[79] P. Hohenberg and W. Kohn, Inhomogeneous electron gas, Phys. Rev. **136**, B864 (1964).

[80] C. Fiolhais, F. Nogueira, and M. A. L. Marques, *A Primer in Density Functional Theory*, Lecture Notes in Physics Vol. 620 (Springer Berlin, Heidelberg, 2003).

[81] M. J. van Setten, M. Giantomassi, E. Bousquet, M. J. Verstraete, D. R. Hamann, X. Gonze, and G.-M. Rignanese, The PSEUDODOJO: Training and grading a 85 element optimized norm-conserving pseudopotential table, Comput. Phys. Commun. **226**, 39 (2018).

[82] J. P. Perdew, K. Burke, and M. Ernzerhof, Generalized gradient approximation made simple, Phys. Rev. Lett. **77**, 3865 (1996).

[83] V. I. Anisimov, J. Zaanen, and O. K. Andersen, Band theory and Mott insulators: Hubbard *U* instead of Stoner *I*, Phys. Rev. B **44**, 943 (1991).

[84] H. J. Monkhorst and J. D. Pack, Special points for Brillouin-zone integrations, Phys. Rev. B **13**, 5188 (1976).

[85] W. H. McMaster, N. K. Del Grande, J. Mallett, and J. Hubbell, Compilation of X-ray Cross Sections., Tech. Rep. (California University, Livermore, Lawrence Radiation Lab., 1969).

[86] C. R. Rotundu, S. Jiang, X. Deng, Y. Qian, S. Khan, D. G. Hawthorn, G. Kotliar, and N. Ni, Physical properties and electronic structure of a new barium titanate suboxide $Ba_{1+\delta}Ti_{13-\delta}O_{12}$ ($\delta = 0.11$), APL Mater. **3**, 041517 (2015).

[87] A. K. Gupta, S. Gupta, S. Mandal, and R. Sachan, Laser irradiation-induced nanoscale surface transformations in strontium titanate, Crystals **12**, 624 (2022).

[88] G. Lucovsky, C. C. Fulton, Y. Zhang, Y. Zou, J. Luning, L. F. Edge, J. L. Whitten, R. J. Nemanich, H. Ade, D. G. Schlom *et al.*, Conduction band-edge states associated with the removal of d-state degeneracies by the Jahn-Teller effect, IEEE Trans. Device Mater. Reliab. **5**, 65 (2005).

[89] J. Dai, Y. Zhu, H. A. Tahini, Q. Lin, Y. Chen, D. Guan, C. Zhou, Z. Hu, H.-J. Lin, T.-S. Chan *et al.*, Single-phase perovskite oxide with super-exchange induced atomic-scale synergistic active centers enables ultrafast hydrogen evolution, Nat. Commun. **11**, 5657 (2020).

[90] See Supplemental Material at http://link.aps.org/supplemental/10.1103/PhysRevB.110.235104 for experimental and computational details.

[91] D. E. Barlaz, R. T. Haasch, and E. G. Seebauer, Epitaxial $SrRuO_3/SrTiO_3$ (100) analyzed using x-ray photoelectron spectroscopy, Surf. Sci. Spectra **24**, 024002 (2017).

[92] S. L. Dudarev, G. A. Botton, S. Y. Savrasov, C. J. Humphreys, and A. P. Sutton, Electron-energy-loss spectra and the structural stability of nickel oxide: An LSDA+U study, Phys. Rev. B **57**, 1505 (1998).

[93] F. M. Bickelhaupt, N. J. R. van Eikema Hommes, C. Fonseca Guerra, and E. J. Baerends, The carbon-lithium electron pair bond in $(CH_3Li)_n$ ($n = 1, 2, 4$), Organometallics **15**, 2923 (1996).

[94] Z. Zhong and P. Hansmann, Band alignment and charge transfer in complex oxide interfaces, Phys. Rev. X **7**, 011023 (2017).

[95] P. C. Rogge, P. Shafer, G. Fabbris, W. Hu, E. Arenholz, E. Karapetrova, M. P. Dean, R. J. Green, and S. J. May, Depth-resolved modulation of metal–oxygen hybridization and orbital polarization across correlated oxide interfaces, Adv. Mater. **31**, 1902364 (2019).

[96] J. Suntivich, W. T. Hong, Y.-L. Lee, J. M. Rondinelli, W. Yang, J. B. Goodenough, B. Dabrowski, J. W. Freeland, and Y. Shao-Horn, Estimating hybridization of transition metal and oxygen states in perovskites from O *K*-edge x-ray absorption spectroscopy, J. Phys. Chem. C **118**, 1856 (2014).

[97] R. Nakajima, J. Stöhr, and Y. U. Idzerda, Electron-yield saturation effects in *L*-edge x-ray magnetic circular dichroism spectra of Fe, Co, and Ni, Phys. Rev. B **59**, 6421 (1999).

[98] I. I. Mazin and D. J. Singh, Electronic structure and magnetism in Ru-based perovskites, Phys. Rev. B **56**, 2556 (1997).

[99] W. Siemons, G. Koster, A. Vailionis, H. Yamamoto, D. H. A. Blank, and M. R. Beasley, Dependence of the electronic structure of $SrRuO_3$ and its degree of correlation on cation off-stoichiometry, Phys. Rev. B **76**, 075126 (2007).

[100] B. Dabrowski, O. Chmaissem, P. W. Klamut, S. Kolesnik, M. Maxwell, J. Mais, Y. Ito, B. D. Armstrong, J. D. Jorgensen, and S. Short, Reduced ferromagnetic transition temperatures in $SrRu_{1-v}O_3$ perovskites from Ru-site vacancies, Phys. Rev. B **70**, 014423 (2004).

[101] A. J. Grutter, F. J. Wong, E. Arenholz, A. Vailionis, and Y. Suzuki, Evidence of high-spin Ru and universal magnetic anisotropy in $SrRuO_3$ thin films, Phys. Rev. B **85**, 134429 (2012).

[102] H. Jeong, S. G. Jeong, A. Y. Mohamed, M. Lee, W.-S. Noh, Y. Kim, J.-S. Bae, W. S. Choi, and D.-Y. Cho, Thickness-dependent orbital hybridization in ultrathin $SrRuO_3$ epitaxial films, Appl. Phys. Lett. **115**, 092906 (2019).

[103] G. Fabbris, D. Meyers, J. Okamoto, J. Pelliciari, A. S. Disa, Y. Huang, Z.-Y. Chen, W. B. Wu, C. T. Chen, S. Ismail-Beigi, C. H. Ahn, F. J. Walker, D. J. Huang, T. Schmitt, and M. P. M. Dean, Orbital engineering in nickelate heterostructures driven by anisotropic oxygen hybridization rather than orbital energy levels, Phys. Rev. Lett. **117**, 147401 (2016).

[104] B. T. Thole and G. van der Laan, Branching ratio in x-ray absorption spectroscopy, Phys. Rev. B **38**, 3158 (1988).

[105] B. T. Thole and G. van der Laan, Linear relation between X-ray absorption branching ratio and valence-band spin-orbit expectation value, Phys. Rev. A **38**, 1943 (1988).

[106] G. van der Laan and B. T. Thole, Local probe for spin-orbit interaction, Phys. Rev. Lett. **60**, 1977 (1988).

[107] M. A. Laguna-Marco, D. Haskel, N. Souza-Neto, J. C. Lang, V. V. Krishnamurthy, S. Chikara, G. Cao, and M. van Veenendaal, Orbital magnetism and spin-orbit effects in the electronic structure of $BaIrO_3$, Phys. Rev. Lett. **105**, 216407 (2010).

[108] S. Mazumdar, Valence transition model of the pseudogap, charge order, and superconductivity in electron-doped and hole-doped copper oxides, Phys. Rev. B **98**, 205153 (2018).